# Radiation-Preserving Selective Imaging for Pediatric Hip Dysplasia: A Cross-Modal Ultrasound-Xray Policy with Limited Labels

Duncan Stothers<sup>2</sup>, Ben Stothers<sup>1</sup>, Emily Schaeffer<sup>1</sup>, Kishore Mulpuri<sup>1</sup>

<sup>1</sup>Hippy lab, University of British Columbia <sup>2</sup>Independent Researcher, duncanstothers@alumni.harvard.edu

#### Abstract

We study an ultrasound-first, radiation-preserving policy for developmental dysplasia of the hip (DDH) that requests a radiograph only when needed.

We (i) pretrain modality-specific encoders (ResNet-18) with SimSiam on a large unlabelled registry (37,186 ultrasound; 19,546 radiographs), (ii) freeze the backbones and fit small, measurement-faithful heads on DDH relevant landmarks and measurements (iii) calibrate a one-sided conformal deferral rule on ultrasound predictions that provides finite-sample coverage guarantees under exchangeability, using a heldout calibration set. Ultrasound heads predict Graf  $\alpha/\beta$  and femoral head coverage; X-ray heads predict acetabular index (AI), center-edge (CE) angle and IHDI grade. On our held out labeled evaluation set, ultrasound measurement error is modest (e.g.,  $\alpha$  MAE  $\approx 9.7^{\circ}$ , coverage MAE  $\approx 14.0\%$ ), while radiographic probes achieve AI and CE MAEs of  $\approx 7.6^{\circ}$  and  $\approx 8.9^{\circ}$ , respectively. The calibrated US-only policy is explored across rule families (alpha-only; alpha OR coverage; alpha AND coverage), uncertainty inflation factors, and perutility trade-offs using decision-curve analysis. Conservative settings yield high coverage (e.g.,  $\sim$ 0.90 for  $\alpha$ ) with nearzero US-only rates; permissive settings (e.g., alpha OR coverage at larger deltas) achieve non-zero US-only throughput with expected coverage trade-offs.

The result is a simple, reproducible pipeline that turns limited labels into interpretable measurements and tunable selective imaging curves suitable for clinical handoff and future external validation.

### **Background**

Clinical context and age-aware measurements. Developmental dysplasia of the hip (DDH) spans acetabular undercoverage through dislocation across infancy and early childhood. In the radiographic domain, clinically accepted measurements include the acetabular index (AI), IHDI grading, and, when ossification permits, the lateral center-edge (Wiberg) angle and Sharp's acetabular angle (Tönnis 1987; Narayanan et al. 2015; Doski, Qadir et al. 2022; Sharp 1961; Wiberg 1939). In early infancy, standardized sonography under the Graf method (reporting  $\alpha/\beta$  angles and femoral head coverage) is the dominant screening and early management tool (Graf 1980; Graf, Scott, and Lercher 2006; Zieger

Copyright © 2026, Association for the Advancement of Artificial Intelligence (www.aaai.org). All rights reserved.

1986; Omeroğlu 2014). As ossification progresses, anteroposterior (AP) pelvic radiographs become more informative for acetabular development and surgical planning; minimizing ionizing exposure in pediatrics motivates selective XR acquisition (Keller and Nijs 2009; Dezateux and Rosendahl 2007).

Ultrasound-only automation (what exists). A substantial body of work automates hip ultrasound tasks: standardplane detection, quality gating, Graf typing, and direct prediction of  $\alpha/\beta$  and femoral head coverage. Representative approaches include multitask CNNs that jointly detect plane adequacy and infer Graf measurements (Chen et al. 2022: Hu et al. 2022), lightweight real-time systems designed for point-of-care guidance (Hsu, Lin et al. 2025), and pipelines that integrate structure/landmark cues to improve robustness (Kinugasa, Kobayashi et al. 2023; Chen et al. 2024). Reviews of pediatric MSK ultrasound emphasize ultrasound's safety, accessibility, and the potential for AI-assisted standardization to reduce operator dependence (van Kouswijk, Yeung, and Jaremko 2025). These methods typically optimize unimodal accuracy/MAE and, when evaluated, report agreement with expert sonographers on Graf measures and coverage.

Radiograph-only automation (what exists). On AP pelvic radiographs, deep systems tackle triage, landmark detection, and explicit measurement prediction for AI, CE, and related angles. Recent efforts use local-global architectures and landmark-aware heads to increase interpretability and reduce measurement bias (Liu et al. 2020; Moon et al. 2024; Li et al. 2019). Additional work frames DDH classification and grading tasks with CNNs and detectors (Park et al. 2021; Zhang et al. 2020; Fraiwan et al. 2022; Den et al. 2023; Xu et al. 2022). Systematic reviews synthesize steady progress but highlight the need for stronger labeling protocols, external validation, and reporting of clinically meaningful measurement error rather than only image-level accuracy (Wu, Wang et al. 2023; Chen, Wang et al. 2024).

Cross-modal US-XR learning (what remains sparse). Despite mature unimodal pipelines, explicitly *paired* US-XR learning for DDH is scarce. Reviews note limited availability of temporally matched US-XR cohorts, inconsistent annotation schemes across modalities, and few methods that directly model the decision of whether to acquire an XR

given a US (Wu, Wang et al. 2023; Chen, Wang et al. 2024; van Kouswijk, Yeung, and Jaremko 2025). Emerging resources begin to address pairing and benchmarking (Qi, Zhang et al. 2025), and there are early bimodal/local-global ideas in related orthopedic settings (Shimizu, Tsukagoshi et al. 2024), but a practical, measurement-aware policy that trades radiation against risk with explicit guarantees remains underexplored.

Why the intersection matters: clinical and statistical rationale. US and XR encode overlapping-but not identicalmorphology. Graf  $\alpha$  and femoral head coverage on US reflect acetabular roof orientation and femoral containment in early infancy, while AI/CE on XR quantify acetabular slope and lateral coverage once ossification permits reliable landmarks (Graf 1980; Graf, Scott, and Lercher 2006; Tönnis 1987; Wiberg 1939). Clinically, a clearly normal US (e.g., high  $\alpha$ , adequate coverage) often reduces the immediate value of XR in very young infants, whereas abnormal or borderline US increases the value of XR to confirm severity, assess symmetry, and plan management. Statistically, this suggests a selective acquisition problem: use US-derived measurements and calibrated uncertainty to predict whether XR would meaningfully shift the diagnostic or management decision boundary.

From ultrasound to radiographic surrogates (US 

XR prediction). Several radiographic targets admit physiologic surrogates on ultrasound. Elevated  $\alpha$  and adequate coverage reduce the likelihood of elevated AI or pathologic IHDI in age-appropriate cohorts; conversely, low  $\alpha$  or poor coverage raise suspicion for acetabular underdevelopment that XR can quantify with AI/CE more precisely as ossification progresses. A measurement-aware proxy model can therefore (i) estimate XR-relevant risk from US measurements, (ii) calibrate one-sided lower bounds that certify "confidently normal" cases against clinical thresholds (e.g.,  $\alpha \ge 60^{\circ}$ ; coverage  $\ge 50\%$ ), and (iii) defer to XR when uncertainty or predicted abnormality exceeds a tunable margin. This framing preserves interpretability (decisions ride on named measurements) and keeps the bridge between modalities clinically legible.

Decision-theoretic selective imaging and risk control. Selective acquisition can be cast as a utility-optimization under uncertainty: balance a (small) radiation cost against the (potentially large) cost of missing a lesion that XR would reveal. In deployment, finite-sample guarantees matter. Conformal prediction provides distribution-free coverage control for one-sided bounds on US measurements, enabling US-only decisions to meet target coverage while routing ambiguous cases to XR. Decision-curve analysis then summarizes net benefit across utility weights, exposing operating points along the safety-radiation frontier.

**Positioning of this work.** We contribute a pragmatic, label-efficient cross-modal policy: (1) self-supervised pretraining on large unlabeled US/XR registries with frozen backbones; (2) small, measurement-faithful heads trained on a curated set of paired studies; (3) a one-sided conformal layer that certifies "US-only" decisions against clini-

cally standard thresholds; and (4) decision-curve analysis that makes explicit the trade between XR utilization and risk. The intersection we target, using calibrated US measurements to decide when XR adds value, addresses the practical gap highlighted by recent reviews (Wu, Wang et al. 2023; Chen, Wang et al. 2024; van Kouswijk, Yeung, and Jaremko 2025) and complements ongoing efforts in unimodal automation (Park et al. 2021; Zhang et al. 2020; Liu et al. 2020; Moon et al. 2024; Chen et al. 2022; Hu et al. 2022).

## Methods

# Data, pairing, and splits

We assembled a large unlabeled corpus for self-supervised pretraining (US: 37,186; XR: 19,546 grayscale images, resized to  $512 \times 512$  and channel-repeated to 3). For supervised training and policy evaluation, we curated a small, paired subset with trainee line/point annotations and strict side/date matching. We removed frog-lateral and non-AP studies with a fixed set of view and QC rules, which eliminated eight subjects. The resulting labeled set contained 321 images from 75 subjects. To avoid leakage, we used subject-level splits: post-train (30 subjects; 136 images; 34 pairs), calibration (7 subjects; 28 images; including 26 ultrasound images; 7 pairs), and evaluation (38 subjects; 157 images; 40 pairs). The strict evaluation set (side-matched US-XR) provided 77 hips with XR ground truth (AI and/or CE and/or IHDI).

For each US image, the trainee recorded a horizontal baseline and  $\alpha/\beta$  lines, exposed/total femoral-head lengths, and an optional ossific-nucleus point. For each XR image, the trainee recorded Hilgenreiner's H-line, Perkin's P-line, a  $45^\circ$  reference, the H-point, an acetabular index line, and CE-angle rays, with laterality handled explicitly. Numeric targets were derived by the standard acute-angle and ratio formulas (Graf  $\alpha/\beta$ ; coverage = exposed/total; AI = angle(H-line, AI-line); CE = angle(vertical, CE-ray); IHDI from the quadrant of the H-point).

# Self-supervised pretraining (SimSiam) and frozen encoders

We train separate encoders for US and XR with SimSiam on the unlabeled corpora and then freeze them. Let  $f_{\phi}$  be a ResNet-18 encoder,  $h_{\phi}$  a projection MLP, and  $q_{\phi}$  a prediction MLP. For an image x, we draw two augmentations  $t_1, t_2$  to obtain views  $v_1 = t_1(x)$  and  $v_2 = t_2(x)$ . Define

$$z_1 = h_{\phi}(f_{\phi}(v_1)), \quad z_2 = h_{\phi}(f_{\phi}(v_2)),$$
  
 $p_1 = q_{\phi}(z_1), \quad p_2 = q_{\phi}(z_2).$ 

The SimSiam loss is the stop-gradient negative cosine similarity:

$$\mathcal{L}_{\text{SSL}}(x;\phi) = -\frac{1}{2} \left[ \frac{\langle p_1, \, \operatorname{sg}(z_2) \rangle}{\|p_1\|_2 \, \|\operatorname{sg}(z_2)\|_2} + \frac{\langle p_2, \, \operatorname{sg}(z_1) \rangle}{\|p_2\|_2 \, \|\operatorname{sg}(z_1)\|_2} \right].$$

We train for 10 epochs per modality with standard SimSiam augmentations (random crop/flip, color jitter for XR toned down for US), then discard  $h_\phi, q_\phi$  and freeze the encoder  $f_\phi$  for downstream use.

#### Measurement heads on frozen encoders

Given a frozen modality-specific encoder  $f_{\phi}$ , we extract a 512-dimensional feature  $u=f_{\phi}(x)$  (global average pooled). We then fit small, measurement-faithful heads with task-appropriate losses.

**Ultrasound head.** We use a single MLP with one hidden layer (128 units) and three outputs predicting  $\hat{\alpha}, \hat{\beta} \in \mathbb{R}$  (degrees) and  $\widehat{\text{cov}} \in \mathbb{R}$  (percentage points). Let  $y^{\alpha}, y^{\beta}, y^{\text{cov}}$  denote the trainee labels for a given image. The US loss is mean absolute error (MAE) with per-task scaling to balance magnitudes:

$$\mathcal{L}_{\mathrm{US}}(x) = \lambda_{\alpha} \left| \hat{\alpha} - y^{\alpha} \right| + \lambda_{\beta} \left| \hat{\beta} - y^{\beta} \right| + \lambda_{\mathrm{cov}} \left| \widehat{\mathrm{cov}} - y^{\mathrm{cov}} \right|.$$

In our implementation we set  $\lambda_{\alpha} = \lambda_{\beta} = 1$  and  $\lambda_{cov} = 1$  (coverage reported in percentage points).

**Radiograph heads.** We fit angle regressors for AI and CE and, when present, an IHDI classifier. Let  $\hat{a}, \hat{e} \in \mathbb{R}$  be AI and CE predictions and  $\hat{\pi} \in \Delta^{K-1}$  be softmax probabilities over K IHDI grades. With angle labels  $y^{\rm AI}, y^{\rm CE}$  and (optional) IHDI one-hot  $y^{\rm IHDI}$ ,

$$\mathcal{L}_{XR}(x) = \mu_{AI} \left| \hat{a} - y^{AI} \right| + \mu_{CE} \left| \hat{e} - y^{CE} \right|$$
$$+ \mu_{IHDI} \operatorname{cross\_entropy}(\hat{\pi}, y^{IHDI}),$$

where the crossentropy term is dropped if  $y^{\rm IHDI}$  is absent. In all experiments we set  $\mu_{\rm AI}=\mu_{\rm CE}=\mu_{\rm IHDI}=1$ , i.e., we use an unweighted sum of the available terms. When  $y^{\rm IHDI}$  is missing, the classification term is omitted rather than reweighted. Given the limited dataset size and the relatively similar numeric scale of AI and CE errors, we did not attempt further loss reweighting. We train heads on the post-train split only and select by validation MAE (angles) and accuracy (IHDI) on the calibration subset, then freeze heads for evaluation and policy analysis.

# Calibration: affine bias correction and one-sided conformal bands

For selective imaging we require calibrated lower bounds on US measurements so that "US-only" decisions meet finite-sample coverage. We perform two steps on the US calibration set  $\mathcal{C} = \{(x_i, y_i)\}$  for each target  $t \in \{\alpha, \text{cov}\}$ .

(i) Affine bias correction. Let  $\hat{y}_i^t$  be the head prediction on  $x_i$ . We fit a robust affine correction

$$\begin{split} \tilde{y}_i^t &= a_t \, \hat{y}_i^t \, + \, b_t \\ \text{by} \quad (a_t, b_t) &\in \arg \min_{a, b} \, \sum_{(x_i, y_i) \in \mathcal{C}} \left| a \, \hat{y}_i^t + b - y_i^t \right|. \end{split}$$

This reduces small systematic bias without re-training the head.

(ii) One-sided residual quantiles. Define residuals  $r_i^t=y_i^t-\tilde{y}_i^t.$  For a desired miscoverage level  $\rho\in(0,1)$  we compute a one-sided conformal radius

$$q_t^+(\rho) = \text{Quantile}_{1-\rho} \Big( -r_i^t \text{ over } (x_i, y_i) \in \mathcal{C} \Big),$$

so that, under exchangeability, with probability  $\geq 1-\rho$  a fresh sample will satisfy  $y^t \geq \tilde{y}^t - q_t^+(\rho)$ . We introduce a tunable inflation factor  $\delta_t \geq 0$  to explore conservative settings:

$$LB_t(x; \rho, \delta_t) = \tilde{y}^t(x) - (1 + \delta_t) q_t^+(\rho).$$

Here  $\delta_t$  is swept on a discrete grid (e.g., 0.10:0.40) to produce coverage-utilization curves.

# **Selective imaging rules (US-only vs. defer to XR)**

Let  $T_{\alpha}$  and  $T_{\rm cov}$  denote clinical normality thresholds (we use  $T_{\alpha}{=}60^{\circ}$  and  $T_{\rm cov}{=}50\%$ ). For an evaluation US image x, we declare "US-only" if the calibrated lower bounds exceed thresholds. We study three rule families:

### Alpha-only

$$d_{\alpha}(x) = \mathbb{I}[LB_{\alpha}(x; \rho, \delta_{\alpha}) \ge T_{\alpha}].$$
 (1)

#### Alpha OR Coverage

$$d_{\alpha \vee \text{cov}}(x) = \mathbb{I}[\text{LB}_{\alpha}(x; \rho, \delta_{\alpha}) \ge T_{\alpha} \vee \text{LB}_{\text{cov}}(x; \rho, \delta_{\text{cov}}) > T_{\text{cov}}]. \quad (2)$$

# Alpha AND Coverage

$$d_{\alpha \wedge \text{cov}}(x) = \mathbb{I}[\text{LB}_{\alpha}(x; \rho, \delta_{\alpha}) \ge T_{\alpha} \wedge \text{LB}_{\text{cov}}(x; \rho, \delta_{\text{cov}}) \ge T_{\text{cov}}]. \quad (3)$$

Here  $d(\cdot) \in \{0,1\}$  indicates "US-only" (1) vs. "defer to XR" (0). For  $\rho$  fixed (we use  $\rho$ =0.10), sweeping  $(\delta_{\alpha}, \delta_{\rm cov})$  yields a grid of policies.

**Ossification-proxy variant.** As a pragmatic sensitivity analysis, we also evaluate a variant that conditions thresholds on an ossific-nucleus flag  $o \in \{0,1\}$  (from the US point annotation), e.g.,

$$T_{\alpha}(o) = \begin{cases} 60^{\circ}, & o = 0 \\ 60^{\circ}, & o = 1 \end{cases} T_{\text{cov}}(o) = \begin{cases} 50\%, & o = 0 \\ 50\%, & o = 1 \end{cases}$$

(kept equal in this study, but the machinery supports *o*-specific thresholds). This lets future work explore age/ossification-aware tuning without altering the conformal recipe.

# Pair construction and XR ground-truth events

To align US decisions with XR outcomes, we form strict pairs on the evaluation split using (subject, date, side). For each pair j, define a binary XR abnormality indicator  $z_j \in \{0,1\}$  that aggregates available radiographic ground truth (e.g., thresholding AI or CE when present, or using IHDI grades). We report all computations both per-rule and per- $(\delta_{\alpha},\delta_{\text{cov}})$  on the subset with at least one XR label.

# **Empirical coverage and safety diagnostics**

On the evaluation US set  $\mathcal{E}$  we compute empirical one-sided coverage for each target,

$$\widehat{\operatorname{cov}}_t = \frac{1}{|\mathcal{E}|} \sum_{(x,y)\in\mathcal{E}} \mathbb{I}[y^t \ge \operatorname{LB}_t(x; \rho, \delta_t)], \quad t \in \{\alpha, \operatorname{cov}\}.$$

We also report miss rate among US-only decisions, MR =  $\frac{\sum_j d_j z_j}{\sum_j d_j}$ , and the US-only rate,  $\text{UOR} = \frac{1}{N} \sum_j d_j$ , where N is the number of strict pairs.

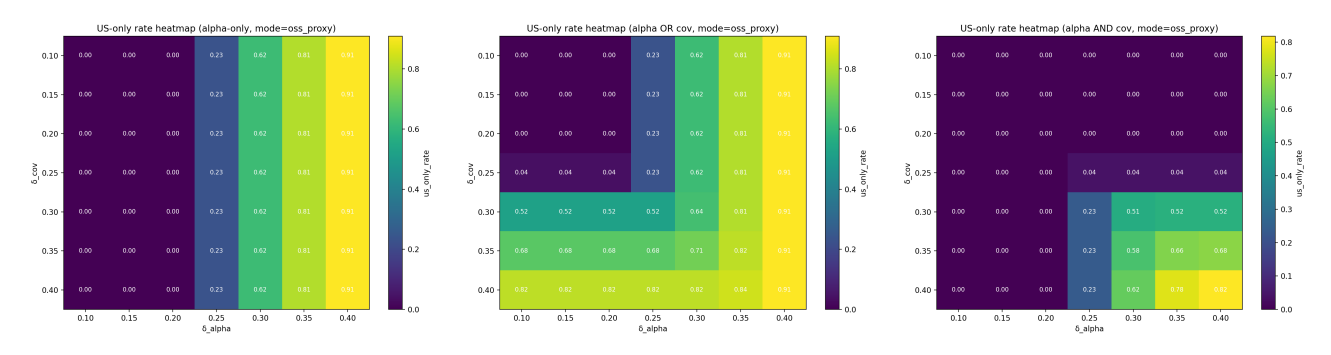


Figure 1: US-only rate across  $(\delta_{\alpha}, \delta_{cov})$  for the three policy families.

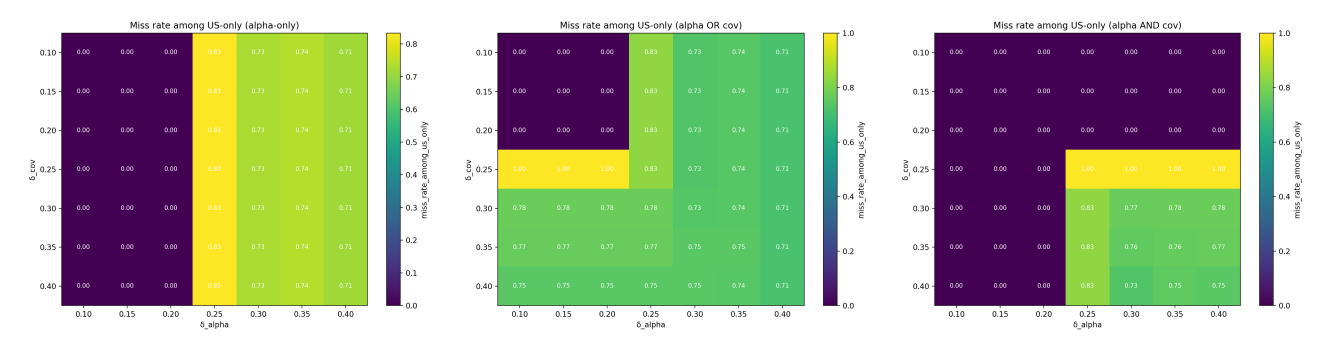


Figure 2: Miss rate among US-only decisions across the same grid.

# Decision-curve analysis (utility over cost-penalty grids)

To summarize policy desirability across clinical preferences, we define a simple per-pair utility with radiation cost  $\lambda \geq 0$  and miss penalty  $\mu \geq 0$ :

$$u_j(d_j; \lambda, \mu, z_j) = -\lambda (1 - d_j) - \mu z_j d_j.$$

Acquiring XR  $(d_j=0)$  incurs cost  $\lambda$ ; skipping XR  $(d_j=1)$  risks a penalty  $\mu$  if the case is XR-abnormal  $(z_j=1)$ . The average utility for a policy family  $\Pi$  over  $(\delta_\alpha, \delta_{\rm cov})$  and strict pairs  $\{1,\ldots,N\}$  is

$$U_{\Pi}(\lambda, \mu) = \max_{(\delta_{\alpha}, \delta_{\text{cov}}) \in \mathcal{G}} \frac{1}{N} \sum_{j=1}^{N} u_{j} (d_{j}(\delta_{\alpha}, \delta_{\text{cov}}); \lambda, \mu, z_{j}),$$

where  $\mathcal{G}$  is the swept grid. We plot  $U_{\Pi}(\lambda,\mu)$  versus  $\lambda$  for fixed  $\mu$  and compare against "acquire-all" and "acquirenone" baselines; this is analogous to net-benefit curves and exposes the radiation-safety trade-off transparently.

# Implementation details

All images were resized to  $512 \times 512$  with aspect-preserving padded crops; grayscale channels were replicated to three to match the ResNet stem. We trained SimSiam for 10 epochs per modality. For supervised heads, we used MAE for angle/coverage targets and cross-entropy for IHDI when labels were present; heads were trained on *post-train* only, tuned on *calibration*, and evaluated on *evaluation*. Encoders remained frozen throughout, aligning with the limited-label regime. Conformal calibration used  $\rho$ =0.10 and the

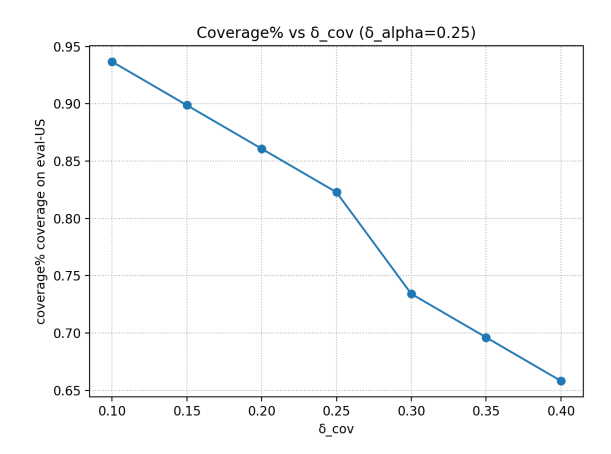
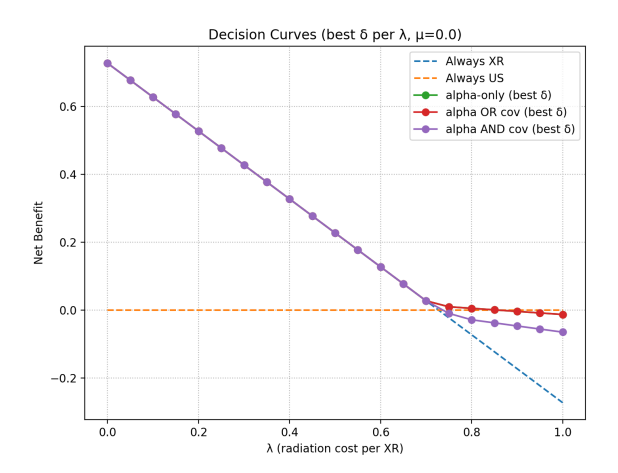


Figure 3: Empirical one-sided coverage for femoral head coverage as  $\delta_{\rm cov}$  varies.

affine correction described above; we swept  $\delta_{\alpha}, \delta_{\rm cov} \in \{0.10, 0.15, 0.20, 0.25, 0.30, 0.35, 0.40\}$  to generate the policy grids and figures. Pair construction used strict (subject, date, side) matching; all reported pairwise metrics are computed on the subset with XR ground truth present.



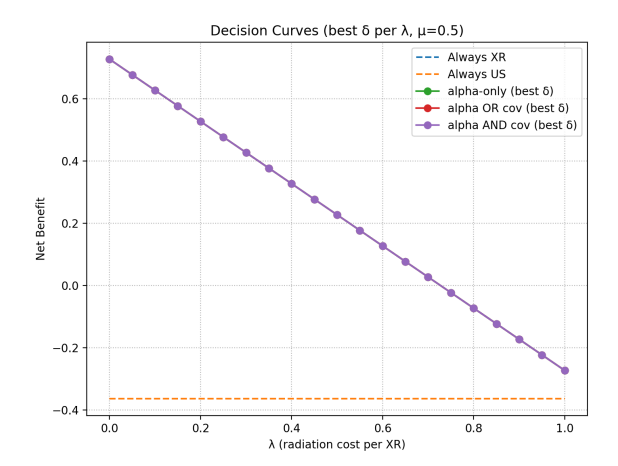


Figure 4: Decision-curve envelopes over radiation cost  $\lambda$  for two miss penalties  $\mu$ .

Table 1: Policy snapshots (strict eval pairs, N=77).

Rule	$\delta_{\alpha}/\delta_{\rm cov}$	US-only	XR use	$cov_{\alpha}$
AND	0.10 / 0.10	0.00	1.00	0.90
AND	0.20 / 0.20	0.00	1.00	0.80
OR	0.35 / 0.35	0.43	0.57	-
OR	0.40 / 0.40	0.55	0.45	-

#### Results

### **Probe Accuracy on Held-Out Evaluation**

Frozen encoders with small measurement heads achieved low double-digit mean absolute error (MAE) on ultrasound and single-digit MAE on radiographs. On the strict evaluation split, ultrasound probes yielded  $\alpha$  MAE  $=9.69^\circ,\,\beta$  MAE  $=11.25^\circ,$  and head-coverage MAE =13.97 percentage points. Radiographic probes achieved acetabular index (AI) MAE  $=7.60^\circ$  and center-edge (CE) MAE  $=8.93^\circ.$  These accuracies are competitive with unimodal reports that use larger bespoke networks, and they are achieved with frozen backbones and limited labels.

# **Conformal Calibration on Ultrasound**

On the calibration split (7 subjects; 26 ultrasound images), we fitted per-target affine bias corrections then computed one-sided residual quantiles ( $\rho$ =0.10). For  $\alpha$  we obtained  $q_{\alpha}^{+}$ =10.75°; for coverage,  $q_{\rm cov}^{+}$ =28.74 percentage points. Calibration MAEs were  $\approx 6.4^{\circ}$  ( $\alpha$ ) and  $\approx 14.9$  percentage points (coverage). These radii define conservative lower bounds used by the policies in the next sections.

# **Selective Imaging Policies: Coverage and Throughput**

We evaluated three ultrasound-first deferral rules on the strict paired set (N=77 hips with any XR ground truth), sweeping uncertainty inflation factors  $\delta_{\alpha}, \delta_{\rm cov} \in \{0.10:0.40\}$ :

**Alpha-only** requests an X-ray unless the calibrated lower bound for  $\alpha$  exceeds  $60^{\circ}$ . **Alpha OR coverage** requests an X-ray unless either the  $\alpha$  lower bound exceeds  $60^{\circ}$  or the coverage lower bound exceeds 50%. **Alpha AND coverage** requests an X-ray unless both lower bounds exceed their thresholds.

Heatmaps of US-only rate (Fig. 1) and miss rate among US-only decisions (Fig. 2) expose the expected trade-offs. At conservative settings (e.g.,  $\delta_{\alpha}{=}\delta_{\rm cov}{=}0.10$ ), the AND rule keeps US-only rate near zero while reaching empirical coverage  $\approx 0.90$  for  $\alpha$  and  $\approx 0.94$  for coverage on the evaluation US set. Permissive settings under the OR rule increase US-only throughput substantially (e.g.,  $\sim 0.43$  at 0.35/0.35 and  $\sim 0.55$  at 0.40/0.40) with corresponding increases in miss-rate heatmap intensity.

#### Coverage as a Function of Conservatism

Figure 3 shows empirical one-sided coverage for femoral head coverage as a function of  $\delta_{\rm cov}$  (with  $\delta_{\alpha}$  fixed to the grid median), confirming monotone behavior with respect to uncertainty inflation. The same pattern holds for  $\alpha$  (not shown to avoid redundancy).

#### **Decision-Curve Analysis**

We summarize the radiation-safety trade using decision-curve style utilities  $U(\lambda,\mu)$  that penalize each radiograph with cost  $\lambda$  and each missed XR abnormality among US-only cases with penalty  $\mu$ . Figure 4 shows the net-benefit envelopes for  $\mu$ =0 and  $\mu$ =0.5, where for each cost level  $\lambda$  we select the best rule and  $(\delta_{\alpha}, \delta_{\rm cov})$  on our grid. When radiation is costly (higher  $\lambda$ ), conservative policies dominate; as  $\lambda$  falls, permissive OR policies outperform by increasing US-only throughput. The acquire-all and acquire-none baselines are included implicitly in the envelope.

### **Policy Snapshots for Reviewer Orientation**

Table 1 lists a few interpretable operating points. Under AND at 0.10/0.10, US-only rate is zero, XR utilization is

unity, and empirical coverage is high ( $\sim 0.90$  for  $\alpha$ ;  $\sim 0.94$  for coverage). Under OR at 0.35/0.35 and 0.40/0.40, US-only throughput increases to  $\sim 0.43$  and  $\sim 0.55$  while XR utilization drops accordingly. These snapshots match the contour gradients in the heatmaps.

#### **Discussion**

From measurements to decisions. Our goal is not to replace radiographs with ultrasound, but to formalize when ultrasound is enough and when an X-ray has positive value of information. The policy operates on named measurements that clinicians already use in practice, then converts them into calibrated lower bounds relative to clinical thresholds. This keeps the model on familiar ground and makes every decision traceable to a small number of interpretable quantities.

Collaborative decision support, not automation. The framework is designed to collaborate with sonographers, radiologists, and pediatric orthopedists. Clinicians retain control of thresholds and operating points through two dials. First, the rule family encodes clinical preference about how to combine evidence from  $\alpha$  and femoral head coverage. Second, the inflation factors  $(\delta_{\alpha}, \delta_{\text{cov}})$  translate appetite for risk into stricter or looser lower bounds. Heatmaps in Figure 1 and Figure 2 are meant to be used as interactive guides during service setup. Teams can choose conservative points that preserve coverage and defer frequently to XR, or permissive points that reduce XR utilization while accepting a controlled increase in miss risk among US-only cases.

Radiation minimization as an explicit objective. Decision curves in Figure 4 make the radiation trade-off explicit. The utility weights  $(\lambda, \mu)$  are not tuned by the model. They are handles for local policy. Sites that place a high cost on radiation will land on conservative regions of the curves where the alpha AND coverage rule dominates and US-only rates are low. Sites that can tolerate a small increase in miss risk will move along the frontier to OR-rule settings that reduce X-ray utilization. This separates modeling from policy and puts radiation stewardship in the hands of the clinical team.

Safety properties and fail-safe behavior. The policy fails safe in two ways. First, one-sided conformal bounds give finite-sample coverage control on the US-only set. Empirical coverage trends in Figure 3 reflect the intended monotonicity as inflation increases. Second, cases near the thresholds route to XR. The pairwise analysis shows that many borderline hips sit within a few degrees of the  $60^{\circ}$  alpha cutoff. Rather than stretching ultrasound to decide these, the system seeks a radiograph. This mirrors how experienced clinicians act under uncertainty.

**Interpretability and auditability by design.** The pipeline keeps the entire reasoning chain visible: line and point annotations, derived measurements, calibrated lower bounds, rule evaluation, and policy outcome. There are no hidden logits or opaque multi-class outputs gating safety-critical actions. This supports prospective quality assurance and after-action review. If a site wants to adjust a

threshold, reweight the utility, or adopt ossification-aware criteria, the change reads like a guideline, not a re-training recipe.

How clinicians can use the figures. The three figure families provide complementary views for deployment. Heatmaps of US-only rate map operational throughput across  $(\delta_{\alpha}, \delta_{\rm cov})$ . Miss-rate heatmaps bound downside risk on the subset of US-only decisions. Decision curves summarize net benefit across radiation costs and highlight policy dominance regions. Together they provide a conservative floor and a permissive ceiling, giving a spectrum of defensible operating points that align with local practice and regulatory constraints.

Strengths relative to prior art. Most prior work treats ultrasound and radiography in isolation, often with black-box classifiers. Our approach uses measurement-faithful heads on both modalities, aligns decisions with long-standing clinical thresholds, and introduces coverage-controlled selective prediction to turn a unimodal estimate into a cross-modal action. This retains clinical vocabulary, supports mixed cohorts with variable ossification, and exposes an explicit safety knob.

Generalization and subgroup reliability. Real deployments will face device heterogeneity, operator variability, and demographic shifts. The conformal layer can be recalibrated per site, per device family, or per age band. Subgroup coverage audits can detect drift and trigger automatic tightening of the inflation factors. Because the policy is measurement-based, these recalibrations are lightweight and do not require end-to-end re-training.

Clinical workflow integration. A practical path is ultrasound-first triage at the point of care. The model computes  $\hat{\alpha}$  and  $\widehat{\text{cov}}$ , applies bias correction, and renders calibrated lower bounds with a simple traffic-light presentation: green for US-only above threshold, gray for defer to XR, and an explanation panel showing the margin to threshold and the chosen  $(\delta_{\alpha}, \delta_{\text{cov}})$ . Radiographs, when acquired, feed back into the registry and enlarge future calibration pools. This supports continuous learning while keeping the clinician in the loop.

**Future work.** Three extensions are natural. First, add modality-specific quality gates and age or ossification-aware thresholds so the rule respects validity domains automatically. Second, explore US→XR surrogates that predict radiographic AI or IHDI risk from ultrasound measurements, then fold those calibrated risks into the decision curves. Third, run a prospective study that measures radiation saved per 100 infants, change in return-visit rates, and agreement with multidisciplinary adjudication. Each of these fits within the current policy scaffold without sacrificing interpretability.

**Conclusion.** This study shows that a small set of measurement-faithful probes, a calibration step that controls coverage, and a transparent policy grid are sufficient to build a collaborative assistant for selective imaging in DDH. The assistant is tunable to local radiation preferences, deferential

near uncertainty, and legible to the clinicians who must own the decision. The figures and tables are intended as handrails for clinical setup and as a reproducible template for future multi-site validation.

#### References

- Chen, T.; Zhang, Y.; Wang, B.; et al. 2022. Development of a fully automated Graf standard plane selection and measurement method for infant hip ultrasound. *Diagnostics*, 12(2): 488.
- Chen, Y.-P.; Fan, T.-Y.; Chu, C.-J.; Lin, J.-J.; Ji, C.-Y.; Kuo, C.-F.; and Kao, H.-K. 2024. Automatic and human-level Graf's type identification for detecting developmental dysplasia of the hip. *Biomedical Journal*, 47(2): 100614.
- Chen, Z.; Wang, X.; et al. 2024. Application of artificial intelligence in the diagnosis of developmental dysplasia of the hip based on imaging features: a systematic review. *Journal of Orthopaedic Surgery and Research*.
- Den, H.; Koga, H.; Oda, T.; et al. 2023. Diagnostic accuracy of a deep learning model using YOLOv5 for developmental dysplasia of the hip. *Scientific Reports*, 13: 7383.
- Dezateux, C.; and Rosendahl, K. 2007. Developmental dysplasia of the hip. *The Lancet*, 369(9572): 1541–1552.
- Doski, J.; Qadir, R.; et al. 2022. An Upgrade of the International Hip Dysplasia Institute Classification for Developmental Dysplasia of the Hip. *Clinics in Orthopedic Surgery*, 14(1): 1–9.
- Fraiwan, M.; Al-Kofahi, N.; Ibnian, A.; and Hanatleh, O. 2022. Detection of developmental dysplasia of the hip in X-ray images using deep transfer learning. *BMC Medical Informatics and Decision Making*, 22(216).
- Graf, R. 1980. The diagnosis of congenital hip-joint dislocation by the ultrasonic compound treatment. *Archives of Orthopaedic and Traumatic Surgery*, 97(2): 117–133.
- Graf, R.; Scott, S.; and Lercher, K. 2006. *Hip Sonography: Diagnosis and Management of Infant Hip Dysplasia*. Berlin: Springer, 2nd edition.
- Hsu, W.-S.; Lin, Y.-C.; et al. 2025. Real-Time Ultrasound Diagnosis of Developmental Dysplasia of the Hip Using Deep Learning. *International Journal of Medical Sciences*, 22: 4236–4250.
- Hu, X.; Wang, L.; Yang, X.; Zhou, X.; Xue, W.; Cao, Y.; Liu, S.; Huang, Y.; Guo, S.; Shang, N.; Ni, D.; and Gu, N. 2022. Joint Landmark and Structure Learning for Automatic Evaluation of Developmental Dysplasia of the Hip in Ultrasound. *IEEE Journal of Biomedical and Health Informatics*.
- Keller, M.; and Nijs, E. 2009. The role of radiographs and ultrasound in developmental dysplasia of the hip: how good are they? *Pediatric Radiology*, 39(2): 211–220.
- Kinugasa, K.; Kobayashi, A.; et al. 2023. Diagnosis of developmental dysplasia of the hip by ultrasound imaging using deep learning. *Journal of Pediatric Orthopaedics*.
- Li, Q.; Zhong, L.; Huang, H.; et al. 2019. Auxiliary diagnosis of developmental dysplasia of the hip by automated detection of Sharp's angle on standardized anteroposterior pelvic radiographs. *Medicine*, 98(51): e18500.

- Liu, C.; Xie, H.; Zhang, S.; Mao, Z.; Sun, J.; and Zhang, Y. 2020. Misshapen Pelvis Landmark Detection With Local–Global Feature Learning for Diagnosing Developmental Dysplasia of the Hip. *IEEE Transactions on Medical Imaging*, 39(12): 3944–3954.
- Moon, K.; Kim, Y.; Lee, H.; et al. 2024. Automated assessment of pelvic radiographs using deep learning: validation for multiple radiographic parameters. *Heliyon*. Article epublication.
- Narayanan, U.; Mulpuri, K.; Sankar, W.; Clarke, N.; Hosalkar, H.; and Price, C. 2015. Reliability of a New Radiographic Classification for Developmental Dysplasia of the Hip (IHDI classification). *Journal of Pediatric Orthopaedics*, 35(5): 478–484.
- Omeroğlu, H. 2014. Use of ultrasonography in developmental dysplasia of the hip. *Journal of Children's Orthopaedics*, 8(2): 105–113.
- Park, H.; Jeon, K.; Cho, K.; Kim, S.; and Hwang, H. 2021. Diagnostic performance of a convolutional neural network for detecting developmental dysplasia of the hip on anteroposterior pelvic radiographs. *Korean Journal of Radiology*.
- Qi, G.; Zhang, H.; et al. 2025. A dataset for quality evaluation of pelvic X-ray and pelvic landmark detection (MTDDH). https://www.nature.com/articles/s41597-025-05146-x. Scientific Data article; pediatric pelvic radiograph dataset for DDH tasks.
- Sharp, I. 1961. Acetabular Dysplasia: The Acetabular Angle. *Journal of Bone and Joint Surgery. British Volume*, 43-B(2): 268–272.
- Shimizu, H.; Tsukagoshi, R.; et al. 2024. Bimodal machine learning model for unstable hips in infants: integration of radiographic images with automatically generated clinical measurements. *Scientific Reports*.
- Tönnis, D. 1987. Congenital Dysplasia and Dislocation of the Hip in Children and Adults. Berlin: Springer.
- van Kouswijk, H.; Yeung, M.; and Jaremko, J. 2025. Current and Emerging Applications of Artificial Intelligence in Pediatric Musculoskeletal Imaging. *Children*, 12(5): 645.
- Wiberg, G. 1939. Studies on Dysplastic Acetabula and Congenital Subluxation of the Hip Joint: With Special Reference to the Complication of Osteoarthritis. *Acta Chirurgica Scandinavica (Supplement)*, 83(Suppl 58): 7–38.
- Wu, X.; Wang, Y.; et al. 2023. Artificial intelligence for acetabular index measurement and DDH assessment: a systematic review and meta-analysis. *Frontiers in Pediatrics*, 11: 1094892.
- Xu, L.; Zhao, Z.; Wang, L.; et al. 2022. Deep-Learning Aided Diagnostic System in Assessing Developmental Dysplasia of the Hip on Pediatric Pelvic Radiographs. *Frontiers in Pediatrics*, 10: 785480.
- Zhang, Y.; Sun, J.; Zhang, S.; Li, C.; et al. 2020. Artificial intelligence-assisted diagnosis of paediatric developmental dysplasia of the hip using anteroposterior pelvic radiographs. *Bone & Joint Journal*, 102-B(11): 1650–1657.
- Zieger, M. 1986. Ultrasound of the infant hip. Part 2. Validity of the method. *Pediatric Radiology*, 16: 488–492.